Applied Nanoscience (2020) 10:1173–1181
https://doi.org/10.1007/s13204-019-01182-3

ORIGINAL ARTICLE

# Transforming polymorphs of Co-doped $TiO_2$ nanoparticles: an efficient photo-electrode for dye-sensitized solar cells

**R. Jeba Beula[1] · D. Suganthi[2] · A. Abiram[1] · B. Vidhya[1]**

Received: 5 September 2019 / Accepted: 1 October 2019 / Published online: 31 October 2019


## Abstract

Simple sol–gel assisted spin coating technique was used to prepare cobalt-doped $TiO_2$ films for the application of dye-sensitized solar cells (DSSC). $TiO_2$ photo-electrodes with few Co concentrations (0, 0.025, 0.05, 0.075 and 0.1 M) were prepared on conducting glass substrates. The morphology, structure and composition of the Co:$TiO_2$ films were observed using SEM, XRD and EDAX analysis. The average crystallite size of Co:$TiO_2$ nanoparticles obtained from diffractograms are in the range of 3–12 nm. The transformation of polymorphs from anatase to rutile and vice versa for the increasing concentrations of Co in $TiO_2$ films is observed. The values of optical bandgap energy for Co-doped films are observed to be higher than the pure $TiO_2$ film and the highest is for the dopant level of 0.025 M. Doping of 0.1 M Co in $TiO_2$ enhances the power conversion efficiency of DSSC by 65% compared to pure $TiO_2$ film, demonstrating the influence of Co doping on the functioning of DSSC.

**Keywords** Co-doped $TiO_2$ · $TiO_2$ · DSSC · Spin coating technique · Sol–gel

## Introduction

From the time, Grätzel group developed dye-sensitized solar cells (DSSC), a large number of scientists set out much enthusiasm in DSSCs due to their relatively high-solar energy conversion efficiency, flexibility, low cost and less toxicity to the environment. DSSCs are deliberated as a potential replacement to the existing silicon-based solar cells (Jeong and Kim 2011; Umar 2009; Lee et al. 2009). DSSCs consists of a dye sensitizer adsorbed on the surface of a metal oxide nanoparticle with wide bandgap, electrolyte containing redox couples ($I^-/I^{3-}$) and platinum or carbon-based counter electrode (Jin et al. 2010; Lee et al. 2016). Several efforts by various research groups were taken to increase the DSSC performance by means of tuning the above-mentioned components. Among them, the metal oxide nanoparticles (photoanode) play an essential role in influencing the performance of DSSC (Sutanto et al. 2018). Nanoparticles have significant mechanical and electrical properties due to its large surface to volume ratio (Cui et al. 2019a, b; Zhang et al. 2018a). Titanium dioxide ($TiO_2$) nanoparticles have now been widely used as a photoanode for DSSC due to its resilient oxidative potential, stability, high surface area and environment friendly (Rashad et al. 2013; Zhang et al. 2018b). However, the restrictions associated in using $TiO_2$ as a photoanode are its rapid electron transport ability leading to the electron–hole recombination and its absorption ability only in the ultra violet (UV) region of solar radiation (Chen et al. 2010; Stengl and Bakardjieva 2010). To solve these issues, many researchers have worked on process of surface modification of photo-electrodes such as doping using metals and non-metals, semiconductor coupling which emerged to harness wider spectrum of solar radiation with an increase in absorbance of photoanodes as seen in the literature (Tang et al. 2010; Nair et al. 2011). Particularly, inclusion of small amount of impurities (metallic or non-metallic) to $TiO_2$ lattice sites can shift the absorption region to visible range of solar band and can prevent the electron–hole recombination resulting to improve the power conversion efficiency (Yang et al. 2010). Among the metal dopant ions, cobalt has been extensively examined owing to its best optical and magnetic properties. Co ions introduce new defect levels in the surface of $TiO_2$ and hence weaken the rate of electron–hole

✉ R. Jeba Beula
beular@karunya.edu

[1] Karunya Institute of Technology and Sciences, Coimbatore 641114, India

[2] Hindustan Institute of Technology and Science, Chennai 603103, India

recombination (Choudhury and Choudhury 2012). In addition, they can enhance the dye adsorption resulting in the possibility of increasing the photo-conversion efficiency. In this article, we report the cobalt-doped $TiO_2$ as photoanodes for improved performance of DSSCs. The influence of Co on the properties of $TiO_2$ is also investigated.

## Experimental methods

### Preparation of $TiO_2$ film

A fine blocking layer was deposited on the cleaned FTO (fluorine-doped tin oxide) substrates using the solution of titanium isopropoxide and isopropanol to minimize the electron–hole recombination at the FTO/electrolyte interface. Combination of titanium(IV) butoxide ((1 − $X$)M), various concentrations ($X$ = 0, 0.025, 0.05, 0.075, and 0.1 M) of cobalt II acetate tetra hydrate, ethanol (10 ml) and triton x-100 were used to prepare the precursor solution for the deposition of Co-doped $TiO_2$ films. After stirring for 30 min, a blended solution containing ethanol (10 ml), distilled water (10 ml), nitric acid (1 ml), and a small amount of poly ethylene glycol (PEG) was introduced and the stirring was sustained for another 4 h. Deposition of Co-doped $TiO_2$ films on ITO substrates (with blocking layer) was done by spin coating (HOLMARC/HO-TH-05) technique at a rotation speed of 3000 rpm for a period of 30 s succeeded by air-drying for 2 min. The coating cycle was repeated for eight times so as to get the preferred film thickness. Consequently, all the coated films were dried in an open air for 30 min at 100 °C and annealed for 1 h at 450 °C.

### DSSC fabrication

Schematic diagram of a constructed DSSC based on Co:$TiO_2$ film is given in Fig. 1. All the prepared films were soaked in a P2P-Ru {($\eta^6$-*p*-cymene)(4-(pyridine-2-yl)pyrimidin-2-amine) chlororuthenium(II) tetrafluoroborate)} dye for a period of 24 h to facilitate an enhanced dye adsorption on top of the surfaces of the films. This dye was formulated by dispersing 4-(pyridine-2-yl)pyrimidin-2-amine (1 M), dichloro(*p*-cymene)Ru(II)dimer (0.5 M), and $NaBF_4$ (0.5 M) in methanol. The homogenization of the yielded compound was due to the process of slow diffusion of ether in methanol. The DSSC was constructed by fixing together the dye-sensitized Co:$TiO_2$ film (working electrode) and reduced graphene oxide (RGO)-coated ITO plates(counter electrode) with the help of binder clips. A mixture of PEG, acetonitrile, glacial acetic acid (0.6 ml), 1-methyl-3-propylimidazolium iodide (0.3 M), potassium iodide (KI) (0.1 M) and iodine ($I_2$) (0.05 M) was used to prepare a polymer electrolyte and was carefully driven into the gap between the two electrodes.

### Characterization

To confirm the structure and phase, the prepared Co–$TiO_2$ films were characterized in X-ray diffractometer (Shimadzu XRD 6000). Scanning electron micrographs (SEM) were recorded using JEOL JSM6390 equipment to analyze the morphology of the films. Raman spectroscopy measurements were carried out through Raman spectrometer (multiRAM) to analyze the vibrational frequency modes of the films. Optical properties of the films were examined by means of UV–visible spectrometer (JASCO UV–Vis NIR, V-670). Luminescence spectra were recorded using photoluminescence (PL) spectrophotometer (Fluorolog-3) to interpret the optical and electronic properties of the films. Current–voltage characteristics of the cells were investigated with the aid of AM 1.5 solar simulator (Keithley-6517B Electrometer) furnished with 1000 W xenon lamp. The active area of dye adsorbed Co:$TiO_2$ photo-electrodes was selected as 0.25 $cm^2$.

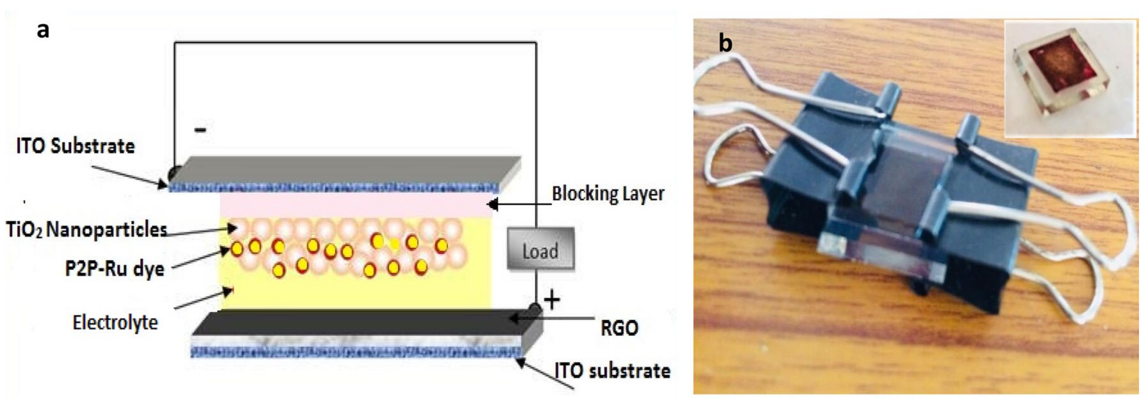


**Fig. 1** **a** Illustration. **b** Optical photos of DSSC

## Results and discussion

Figure 2 indicates the XRD patterns of Co:$TiO_2$ films annealed at 450 °C. The letter "R" represent rutile phase and "A" represent the anatase phase of $TiO_2$. For the pure $TiO_2$ film, the diffraction peaks are obtained at 25.22°, 37.80°, 48.00° and 54.19° coincide with the indices of (101), (004), (200) and (211) planes of anatase $TiO_2$, respectively (JCPDS 75-1537). With the substitution of 0.025 M cobalt, the intensity of anatase phase reduces and the diffraction peaks of rutile phase turn into dominant. However, the rutile phase gradually diminishes and the anatase phase becomes dominant by further increasing the concentrations of Co ions (0.05 M, 0.075 M, and 0.1 M). The diffraction peaks corresponding to rutile phase completely disappear for the Co dopant level of 0.1 M indicating the phase transformation from rutile to anatase phase. Based on the concentration of Co ions, the composition of anatase and rutile phase shows a discrepancy. The phase composition is calculated using the formulas (Spurr and Myres 1957):

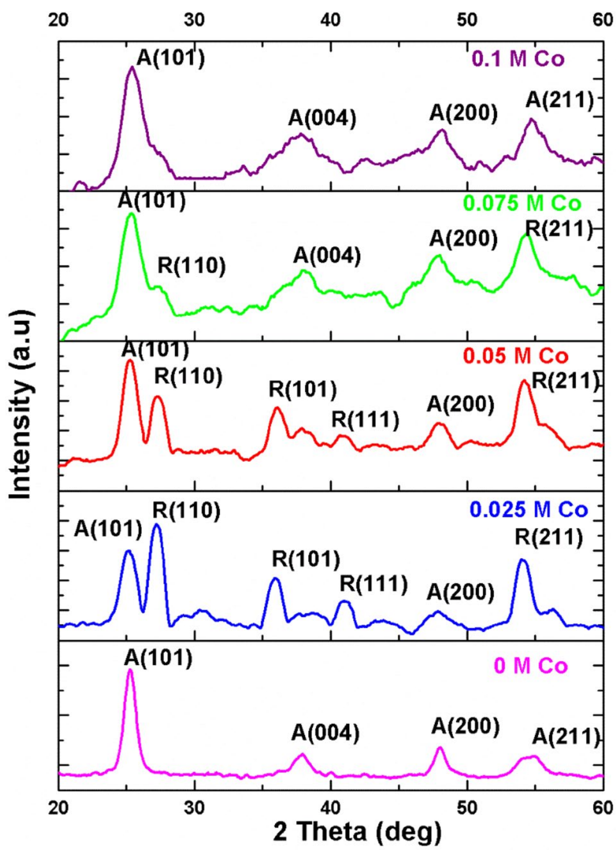


**Fig. 2** XRD patterns Co:$TiO_2$ films

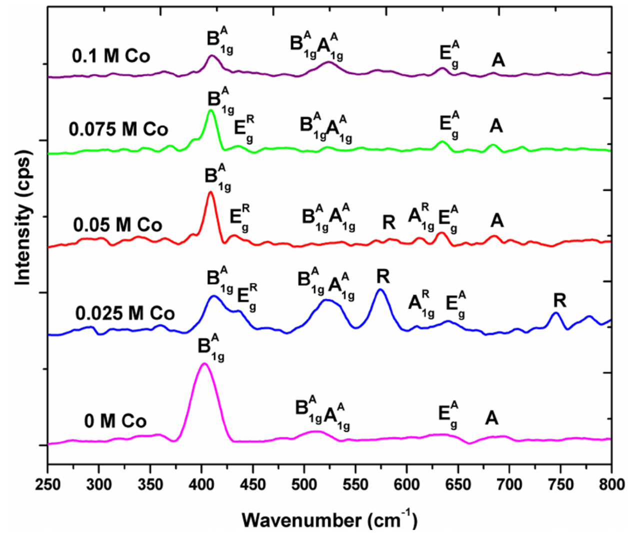


**Fig. 3** Raman spectra of Co:$TiO_2$ films

$$f_a = \frac{1}{1 + 1.26\left(\frac{I_r}{I_a}\right)}, \quad (1)$$

$$f_r = 1 - f_a, \quad (2)$$

where $I_r$—integrated peak intensities of rutile (110) planes $I_a$—integrated peak intensities of anatase (101) planes.

The obtained anatase–rutile phase composition is listed in Table 1. The swinging tendency of polymorphs, anatase to

**Table 1** Structural parameters of Co:$TiO_2$ film

| Doping concentration of cobalt | 2θ (deg) | | Phase composition (%) | | Crystallite size D (nm) | | Average crystallite size D (nm) |
|---|---|---|---|---|---|---|---|
| | Anatase (101) plane | Rutile (110) plane | Anatase (101) plane | Rutile (110) plane | Anatase (101) plane | Rutile (110) plane | |
| 0 | 25.25 | – | 100 | 0 | 8.5 | – | 8.5 |
| 0.025 M | 25.11 | 27.18 | 40.1 | 59.9 | 8.0 | 16.2 | 12.0 |
| 0.05 M | 25.23 | 27.29 | 59.0 | 41.0 | 7.7 | 9.5 | 8.6 |
| 0.075 M | 25.47 | 27.70 | 98.5 | 1.5 | 3.5 | 4.8 | 4.0 |
| 0.1 M | 25.48 | – | 100 | 0 | 3.0 | – | 3.0 |

rutile and again from rutile to anatase transformation is associated to the oxygen vacancies created in $TiO_2$ lattices by the addition of Co ions subject to the ionic radius and valence state of Co (Anupama et al. 2018; Jaiswal et al. 2016). The small and asymmetrical density of Co ions obstructs the nucleation of anatase crystal at the lowest dopant level. An increase in cobalt concentration regularizes the ion distribution and hence enhances the anatase crystallization (Wen-Fan Chen et al. 2016). Based on Hume-Rothery's rules (Hume-Rothery et al. 1940), considerable solubility of solid is favored while the crystal radius of the foreign elements differs by < 15% of that of the host cation. The ionic radius of $Ti^{4+}$ is 74.5 pm and that for $Co^{3+}$ is 75 pm (high spin) and the percentage difference between them is 0.67. Therefore, the $Co^{3+}$ ions have higher solubility in $Ti^{4+}$ and thus the doped films do not show any phase related to cobalt and produce only red shift in the diffraction peak.

The average crystallite sizes of all the prepared Co:$TiO_2$ were determined via Scherer's formula (Cullity and Stock 2001) and are reported in Table 1. The deliberated average size of grains in doped and undoped $TiO_2$ films is found to be in the range from 3 to 12 nm. The crystallite size of

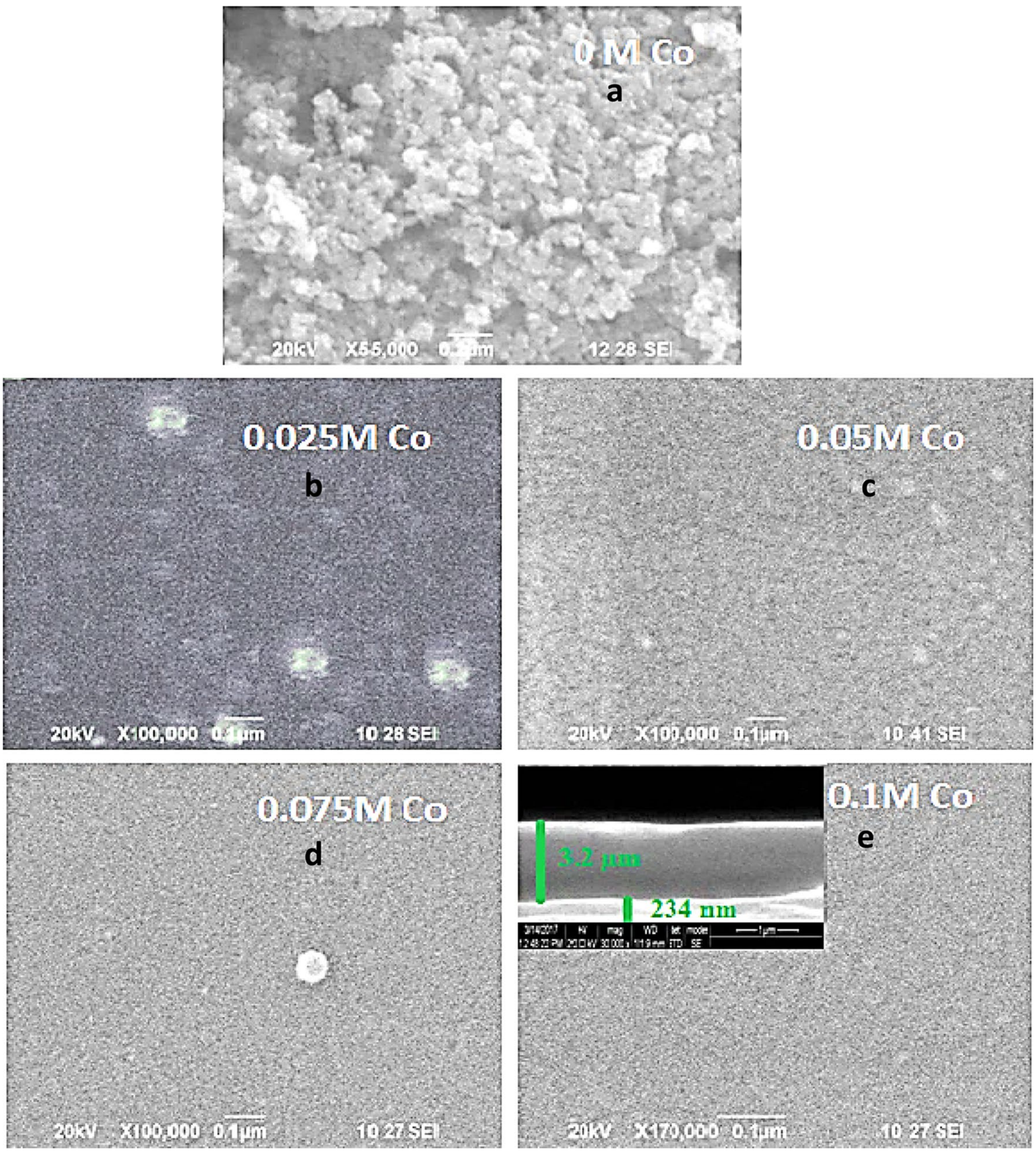


**Fig. 4** SEM images of **a** 0 M, **b** 0.025 M, **c** 0.05 M, **d** 0.075, **e** 0.1 M Co:$TiO_2$ films

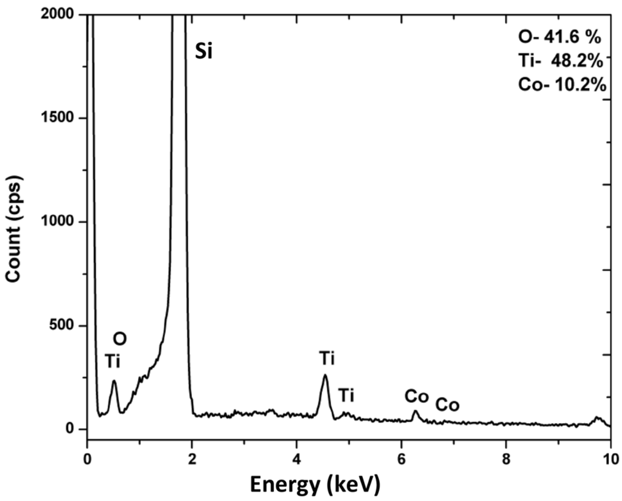


**Fig. 5** EDAX spectra of 0.1 M Co-doped $TiO_2$ film

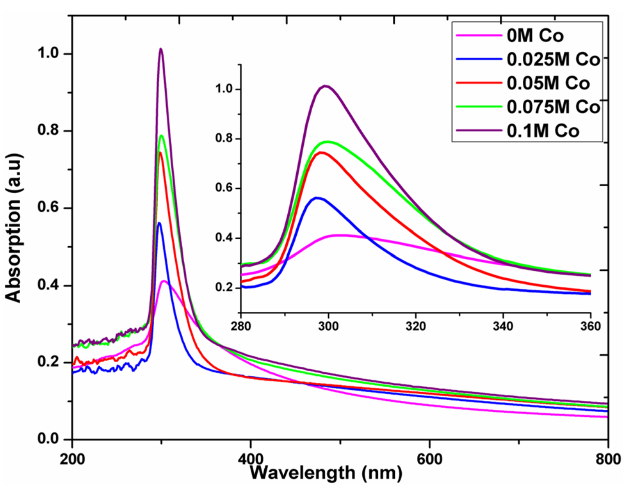


**Fig. 6** Absorption spectra Co:$TiO_2$ films

0.025 M Co-doped $TiO_2$ film shows higher particle size (12 nm) due to the dominancy of rutile phase. The calculated crystallite size of 0.05 M Co doped is found to be the same as pure $TiO_2$ film (~ 8.5 nm) and the size reduces with the increase in dopant concentration. Owing to the smaller size of the particles, all the substituted dopant could not penetrate the $TiO_2$ lattices rather a few Co ions may either assemble on the grain boundaries or on the surfaces, or else they would have gone away from the recognition frame of XRD. The atoms in the grain boundaries stress the periodicity of the lattices of parent material thereby, control the crystal growth and hence decrease in the crystallite size is observed for higher Co concentration (Alamgir et al. 2014).

The Raman spectra of prepared Co:$TiO_2$ films are given in Fig. 3. The pure $TiO_2$ film shows four peaks at 403 $cm^{-1}$ ($B_{1g}$), 512 $cm^{-1}$ ($A_{1g}$), 516 $cm^{-1}$ ($B_{1g}$), and 636 ($E_g$) $cm^{-1}$ with one additional peak at 684 $cm^{-1}$ which are recognized as anatase $TiO_2$ (Ohsaka et al. 1978). Whereas, the Raman spectrum of Co:$TiO_2$ films shows the characteristic peaks related to anatase and rutile phases. An addition of 0.025 M Co during the film formation of $TiO_2$ brings remarkable changes in the Raman spectrum with the presence of characteristic Raman bands for rutile at 436 $cm^{-1}$($E_g$), 574 $cm^{-1}$, 610 $cm^{-1}$ ($A_{1g}$) and 746 $cm^{-1}$ in addition to the anatase $TiO_2$. The dominance of rutile phase is, however, getting reduced upon further addition of Co in $TiO_2$. Three rutile modes at 431 $cm^{-1}$ ($E_g$), 584 $cm^{-1}$, 612 $cm^{-1}$ and four anatase modes at 409 $cm^{-1}$ ($B_{1g}$), 507 $cm^{-1}$ ($A_{1g}$), 517 $cm^{-1}$ ($B_{1g}$) and 634 $cm^{-1}$ ($E_g$) are obtained for 0.05 M Co doping in $TiO_2$ film. Only one rutile mode at 436 $cm^{-1}$ is present in the Raman spectrum of 0.075 M Co-doped $TiO_2$ film. The existence of rutile phase is completely vanished at the doping level of 0.1 M Co in $TiO_2$. Thus, the transformation of two polymorphs of $TiO_2$ upon increasing the dopant concentration has been successfully established from the Raman spectrum and using XRD patterns of the films. Additionally, a trivial red shift is obtained for Co:$TiO_2$ with reference to pure $TiO_2$. This shift in peaks can be ascribed to the lattice stresses ensuing from the existence of Co in $TiO_2$ structure, with lattice expansion directing to the red shift. Due to the decrease in particle size, cobalt-doped $TiO_2$ films reveal peak broadening, reduction in peak intensity and red shift in peak position compared to pure $TiO_2$. When the particle is in nanometer scale, contraction in volume within the particles takes place that leads to the increase in force constant. Owing to the increase in force constant, the Raman bands of Co:$TiO_2$ slightly get shifted to higher wavenumber. Consequently, the variation in the peak intensity of Co:$TiO_2$ is caused by the smaller size of the particles (Choi et al. 2005; Luigi Stagi et al. 2015).

The morphological images of the prepared Co:$TiO_2$ samples are presented in Fig. 4. The SEM images of all the films show the presence of spherical shaped grains and the density of agglomeration of particles increases with increase in the substitution of Co. Comparing the morphology of doped $TiO_2$ with the pure $TiO_2$ film, the former seems to have ultrafine nanoparticles as clearly seen in Fig. 3. Due to considerable neck growth between the particles of Co:$TiO_2$ film, the nanoparticles are closely packed which results in smooth looking surface of doped film. The thickness of the film and the blocking layer measured using the cross-sectional SEM image are found to be 3.2 µm and 234 nm, respectively (insert in Fig. 3e).

Figure 5 displays the EDAX spectrum of 0.1 M Co-doped $TiO_2$ film wherein the peaks of the spectrum tell the presence of Ti, O and Co in the percentages of 48, 42, and 10, respectively, based on atomic weight.

The absorption spectra of prepared films are illustrated in Fig. 6. The maximum absorption peak around 300 nm is obtained for pure $TiO_2$ film. The doping of cobalt in $TiO_2$

shifted the position of the absorption peaks of doped film slightly towards the lower wavelength as shown in the insert of Fig. 6. This shift in the absorption spectra towards blue region is attributed to the familiar quantum size effect of semiconductors for the particles having lesser size (< 10 nm) (Reddy et al. 2002). In addition, substitution of different concentration of cobalt in $TiO_2$ shifts the position of absorption peak bathochromically (0.025 M–297 nm, 0.05 M–298 nm, 0.075 M–300 nm and 0.1 M–299 nm) with respect to the absorption spectrum of pure $TiO_2$ film.

The direct bandgap energy values of the $TiO_2$ films were found using Tauc's relation, $\alpha h\nu = A\,(h\nu - E_g)^n$, where $n = 2$ for direct and $n = ½$ for indirect allowed transitions of the semiconducting materials. The optical bandgap energies were obtained by means of extrapolating the linear part to the energy axis of a $(\alpha h\nu)^2$ vs $h\nu$ graph as pointed in Fig. 7. The direct bandgap energies of prepared $Ti_{(1-x)}Co_xO_2$ ($x = 0$, 0.025, 0.05, 0.75 and 0.1 M) electrodes are found to be 3.31, 3.69, 3.53, 3.36 and 3.43 eV, respectively. The optical bandgap energy values of all the doped films are higher comparing to the pure $TiO_2$ film and the value decreases for higher concentration compared to the lower dopant level (0.025 M). The reduction in bandgap for higher concentration may be due to the interaction of *s*–*p* electrons of $TiO_2$ and *d* electrons of Co.

Figure 8 indicates the PL spectra of the Co:$TiO_2$ films excited at a wavelength of 325 nm. All emission spectra of the films consist of one high intense UV emission band centered at 385 nm related to direct electron–hole recombination and one low intense green emission band with maximum intensity at 510 nm associated to the defects related to the oxygen vacancies created by trapping electrons in the oxygen vacancies (Serpone et al. 1995; Wu et al. 2010). The Gaussian fitting of Co-doped $TiO_2$ films (Fig. 9) shows two peaks: (1) high intense peak at 384 nm for lower concentrations (0.025 M, 0.05 M) and at 386 nm for higher concentrations (0.075 M, 0.1 M) and (2) low intense peak at 476 nm for all the films except 0.025 M Co-doped $TiO_2$ (for which it is obtained at 512 nm). The trivial increase and shift in the peak positions in the PL intensity for 0.025 M Co-doped $TiO_2$ are due to the dominancy of rutile phase (Deborah et al. 2017). From the PL spectra, it is apparent that the Co doping is not bringing any new emission peaks related to $Co^{2+}$ ions but a slight red shifting of near-band emission (NBE) peak position. However, the doping of Co in $TiO_2$ just reduces the PL peak intensity by forming huge quantity of non-radiative

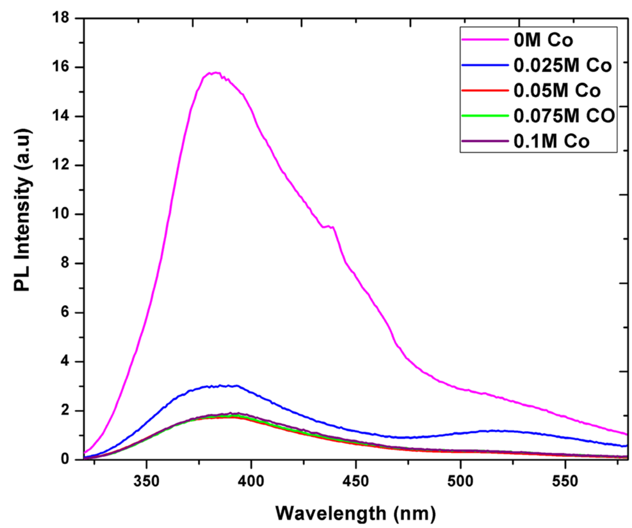


**Fig. 8** PL spectra of Co:$TiO_2$ films

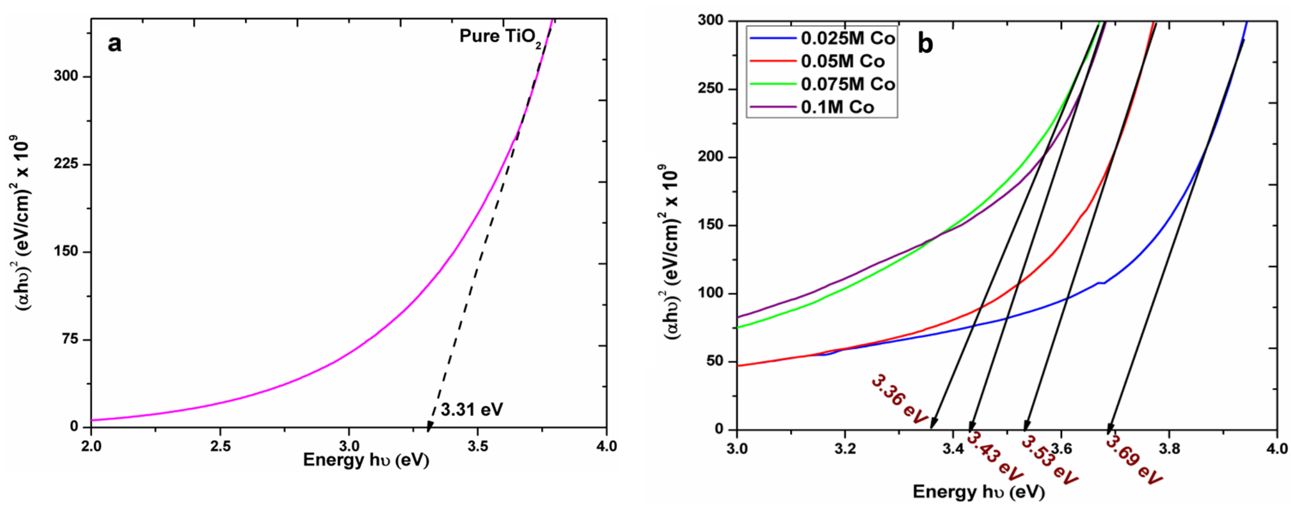


**Fig. 7** Bandgap of **a** pure $TiO_2$ electrode, **b** 0.025 M, 0.05 M, 0.075 M, 0.1 M Co:$TiO_2$ electrodes

centers, which behaves like a luminescent quencher (Xu et al. 2005). In other words, the increase in dopant concentration diminishes the space among active ions, and hence enhances the interaction between them, thereby forming quenching centers. It is to be noted that the highest reduction in intensity of NBE band is observed for the Co:$TiO_2$ films of dopant levels 0.05, 0.075 and 0.1 M. This decrease in emission intensity could also be due to the presence of unbounded Co ions on the grain boundary of $TiO_2$ as already explained in XRD. The lower emission intensity for Co:$TiO_2$ insists the falling of recombination rate, which is a desirable property for increasing the conversion efficiency of DSSC (Choudhury and Choudhury 2012a).

The photovoltaic characteristics of DSSC devices fabricated with pure and doped $TiO_2$ electrodes are shown in Fig. 10 and their *J–V* characteristics are condensed in Table 2. The DSSC fabricated with pure $TiO_2$ shows efficiency ($\eta$) of 1.47%. The efficiency yielded by all the DSSCs made of Co-doped $TiO_2$ are higher than that of the pure $TiO_2$. Substitution of 0.1 M of Co in $TiO_2$ increases the photocurrent conversion efficiency of DSSC to 4.25% with short-circuit current density ($J_{sc}$) of 8.36 mA/cm$^2$, an open-circuit voltage ($V_{oc}$) of 0.82 V, and fill factor (FF) of 0.62 which is about 65% higher than that of pure $TiO_2$ photo-electrode. This increase in efficiency can be ascribed primarily to strong inhibition of electron–hole pair recombination (Xiuquan et al. 2013) which was made evident in PL studies. It is noteworthy that 0.1 M cobalt-doped photoanode has pure anatase phase without the mixing of rutile phase leading to an increase in efficiency of DSSC in contrast to a solar cell with mixed polymorphs of $TiO_2$ (Govindaraj et al. 2015; Park et al. 2000). Since cobalt is a noble conductor, it is having the capability to drive the injected electron faster from the conduction band of $TiO_2$ to ITO substrate

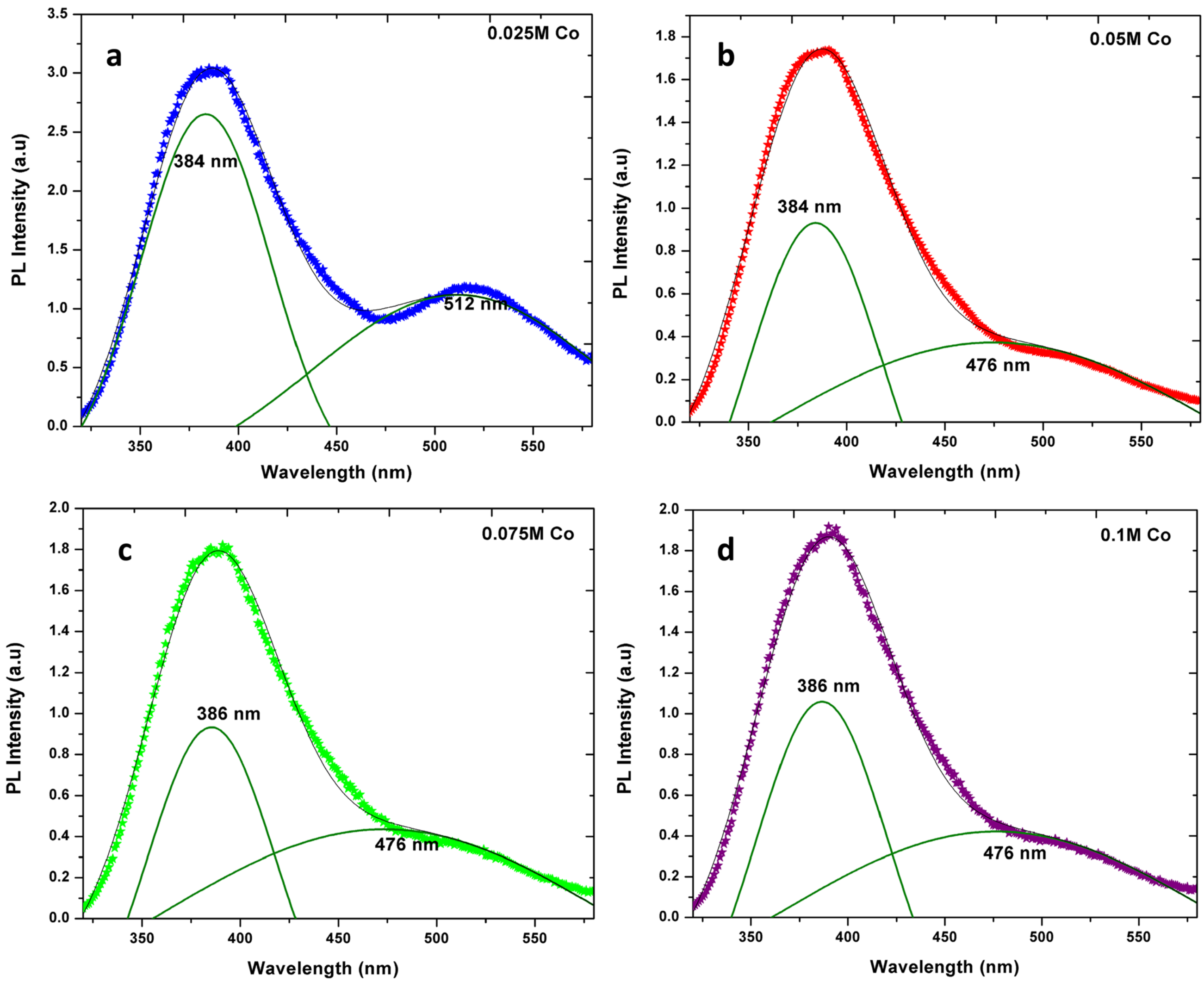


**Fig. 9** Deconvolution of PL spectra of Co:$TiO_2$ films

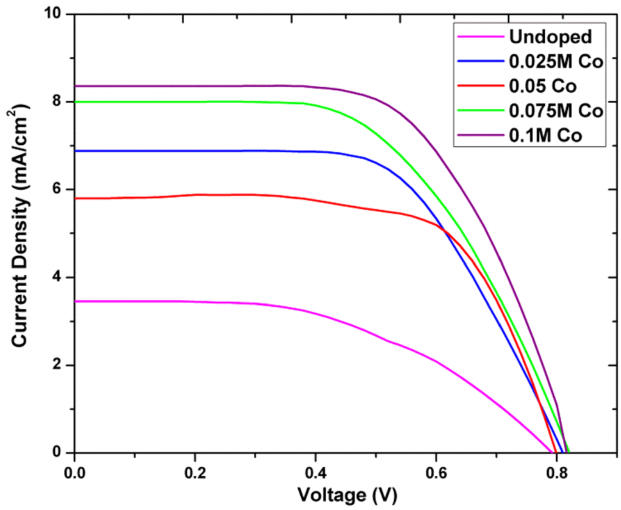


**Fig. 10** *J–V* curve of DSSC with Co:$TiO_2$ films

**Table 2** The photovoltaic parameters of DSSC for pure and Co-doped $TiO_2$ photo-electrodes

| DSSC | $V_{oc}$ (V) | $J_{sc}$ (mA/cm$^2$) | FF | $\eta$ (%) |
|---|---|---|---|---|
| 0 M Co-doped $TiO_2$ | 0.79 | 3.47 | 0.54 | 1.47 |
| 0.025 M Co-doped $TiO_2$ | 0.82 | 6.80 | 0.60 | 3.39 |
| 0.05 M Co-doped $TiO_2$ | 0.79 | 5.80 | 0.69 | 3.16 |
| 0.075 M Co-doped $TiO_2$ | 0.81 | 8.00 | 0.59 | 3.82 |
| 0.1 M Co-doped $TiO_2$ | 0.82 | 8.36 | 0.62 | 4.25 |

inhibiting the chance of recombination with holes. In addition, Co-doped $TiO_2$ photo-electrodes are having adequate amount of electrons for quick reduction of redox electrolyte and ease the transport of injected electron into ITO (Foo Wah Low et al. 2017). The presence of rutile phase in $TiO_2$ films restricts the sensitization of dye and, therefore, reduces an efficiency of DSSC which is because of the lower surface area of rutile than anatase phase (Bakhshayesh and Bakhshayesh 2015). Owing to this reason, DSSC fabricated with lesser amount of anatase phase 0.025 M (anatase 40%) and 0.05 M (59%) Co-doped photo-electrodes shows less power conversion efficiency compared to that of those with higher anatase phase dominated films having Co concentrations of 0.075 M (anatase 98%) and 0.1 M (100%).

## Conclusion

Pure and Co-doped $TiO_2$ photo-electrodes were prepared by means of sol–gel assisted spin coating technique. The influence of cobalt doping in $TiO_2$ was studied using different techniques and the observed properties were found right for increasing the power conversion efficiency of DSSC. A combination of anatase–rutile phase was obtained for the film doped with lower concentration of Co. Complete phase change from rutile to anatase happened at the substitution of 0.1 M doping of Co. The electron–hole recombination rate is highly suppressed by the substitution of Co in $TiO_2$ lattices which is revealed by the PL studies. A higher efficiency of 4.25% was observed for DSSC made with 0.1 M Co-doped $TiO_2$ photo-electrode. Overall, this report demonstrates that Co-doped $TiO_2$ film has prospective scope in boosting the efficiency of DSSC.

## Compliance with ethical standards

**Conflict of interest** On behalf of all the authors, the corresponding author states that there is no conflict of interest.

## References

Alamgir WK, Ahmad S, Hassan MM, Naqvi AH (2014) Structural phase analysis, band gap tuning and fluorescence properties of Co doped $TiO_2$ nanoparticles. Opt Mater 38:278–285

Anupama C, Kumarmani R, Vasundhara M, Joshi SR, Singh J (2018) Structural and magnetic study of undoped and cobalt doped $TiO_2$ nanoparticles. RSC Adv 2018:10939–10947

Bakhshayesh AM, Bakhshayesh N (2015) Enhanced performance of dye-sensitized solar cells aided by Sr, Cr co-doped $TiO_2$ xerogel films made of uniform spheres. J Colloid Interface Sci 460:18–28

Chen SW, Lee JM, Lu KT, Pao CW, Lee JF, Chan TS, Chen JM (2010) Band-gap narrowing of $TiO_2$ doped with Ce probed with X-ray absorption spectroscopy. Appl Phys Lett 97:012104

Chen WF, Koshy P, Huang Y, Adabifiroozjaei E, Yao Y, Sorrell CC (2016) Effect of precipitation, liquid formation, and intervalence charge transfer on the properties and photocatalytic performance of cobalt- or vanadium-doped $TiO_2$ thin films. Int J Hydrog Energy 41:19025–19026

Choi HC, Jung YM, Kim SB (2005) Size effects in the Raman spectra of $TiO_2$ nanoparticles. Vib Spectrosc 37:33–38

Choudhury B, Choudhury A (2012) Luminescence characteristics of cobalt doped $TiO_2$ nanoparticles. J Lumin 132:178–184

Cui J, Zhang Z, Liu D, Zhang D, Wei H, Zou L, Yao L, Zhang C, Huanhuan L, Tang C, Jiang N, Parkin IP, Guo D (2019a) Unprecedented piezoresistance coefficient in strained silicon carbide. Nano Lett 19:6569–6576

Cui J, Zhang Z, Jiang H, Jiang H, Zou L, Guo X, Yao L, Ivan PP, Guo D (2019b) Ultrahigh recovery of fracture strength on mismatched fractured amorphous surfaces of silicon carbide. ACS Nano 13:7483–7492

Cullity BD, Stock SR (2001) Elements of X-ray diffraction, 3rd edn. Prentice Hall, Lawrence

Deborah K, Pallotti LP, Maddalena P, Di Fonzo F, Lettieri S (2017) Photoluminescence mechanisms in anatase and rutile $TiO_2$. J Phys Chem C 121:9011–9021

Govindaraj R, Senthil Pandian M, Ramasamy P, Mukhopadhyay S (2015) Sol–gel synthesized mesoporous anatase titanium dioxide nanoparticles for dye sensitized solar cell (DSSC) applications. Bull Mater Sci 38:291–296

Hume-Rothery W, Smallman RE, Haworth CW (1940) Structure of metals and alloys. J Chem Educ 17:600

Jaiswal R, Patel N, Dashora A, Fernandes R, Yadav M, Edla R, Varma RS, Kothari DC, Ahuja BL, Miotello A (2016) Efficient

Co–B-codoped $TiO_2$ photocatalyst for degradation of organic water pollutant under visible light. Appl Catal B Environ 183:242–253

Jeong JA, Kim HK (2011) Thickness effect of RF sputtered $TiO_2$ passivating layer on the performance of dye-sensitized solar cells. Sol Energy Mater Sol Cells 95:344–348

Jin EM, Park KH, Jin B, Yun JJ, Gu HB (2010) Photosensitization of nanoporous $TiO_2$ films with natural dye. Phys Scr 139:014006

Lee SJ, Cho IH, Kim H, Hong SJ, Lee HY (2009) Microstructure characterization of $TiO_2$ photoelectrodes for dye sensitized solar cell using statistical design of experiments. Trans Electr Electron Mater 10:177–181

Lee M, Balasingam SK, Ko Y, Jeong HY, Min BK, Yun YJ, Jun Y (2016) Graphene modified vanadium pentoxide nanobelts as an efficient counter electrode for dye-sensitized solar cells. Synth Met 215:110–115

Low FW, Lai CW, Hamid SB (2017) Study of reduced graphene oxide film incorporated of $TiO_2$ species for efficient visible light driven dye-sensitized solar cell. J Mater Sci Mater Electron 28:3819–3836

Nair AS, Jose R, Yang S, Ramasrishna S (2011) A simple recipe for an efficient $TiO_2$ nanofiber-based dye-sensitized solar cell. J Colloid Interface Sci 353:39–45

Ohsaka T, Izumi F, Fujiki Y (1978) Raman spectrum of anatase $TiO_2$. J Raman Spectrosc 7:321

Park NG, Van de Lagemaat J, Frank A (2000) Comparison of dye-sensitized rutile-and anatase-based $TiO_2$ solar cells. J Phys Chem B 104:8989–8994

Rashad MM, Shalan AE, Lira-Cantu M, Abdel-Mottaleb MSA (2013) Enhancement of $TiO_2$ nanoparticle properties and efficiency of dye-sensitized solar cells using modifiers. Appl Nanosci 3:167–174

Reddy KM, Manorama SV, Reddy AR (2002) Bandgap studies on anatase titanium dioxide nanoparticles. Mater Chem Phys 78:239

Serpone N, Lawless D, Khairutdinov R (1995) Size effects on the photophysical properties of colloidal anatase $TiO_2$ particles: size quantization versus direct transitions in this indirect semiconductor. J Phys Chem 99:16646–16654

Spurr RA, Myres H (1957) Quantitative analysis of anatase-rutile mixtures with an X-ray diffractometer. Anal Chem 29:760–762

Stagi L, Carbonaro CM, Corpino R, Chiriu D, Ricci PC (2015) Optically controlled phase variation of $TiO_2$ nanoparticles. Phys Status Solidi B 252:1124–1129

Stengl V, Bakardjieva S (2010) Molybdenum-doped anatase and its extraordinary photocatalytic activity in the degradation of orange II in the UV and Vis regions. J Phys Chem C 114:19308–19317

Sutanto B, Arifin Z, Suyitno S (2018) Structural characterisation and optical properties of aluminum-doped zinc oxide nanofibers synthesized by electrospinning. J Eng Sci Technol 13:715–724

Tang YB, Lee CS, Xu J, Liu ZT, Chen ZH, He Z, Cao YL, Yuan G, Song H, Chen L, Luo L, Cheng HM, Zhang WJ, Bello I, Lee ST (2010) Incorporation of graphenes in nanostructured $TiO_2$ films via molecular grafting for dye sensitized solar cell application. J Am Chem Soc 4:3482–3488

Umar A (2009) Growth of comb-like ZnO nanostructures for dye-sensitized solar cells applications. Nanoscale Res Lett 4:1004–1008

Wu WY, Chang YM, Ting JM (2010) Room-temperature synthesis of single-crystalline anatase $TiO_2$ nanowires. Cryst Growth Des 10:1646–1651

Xiuquan GU, Wang B, Zhang Q, Zhao Y, Qiang Y (2013) Preparation of ultrathin $TiO_2$ single-crystal nanowires for high performance dye sensitized solar cells. J Mater Sci Mater Electron 24:520–523

Xu CX, Sun XW, Dong ZL, Tan ST, Cui YP, Wang BP (2005) Manganese-doped zinc oxide tetratubes and their photoluminescent properties. J Appl Phys 98:113513

Yang M, Hume C, Lee S, Son YH, Lee JK (2010) Correlation between photocatalytic efficacy and electronic band structure in hydrothermally grown $TiO_2$ nanoparticles. J Phys Chem C 114:15292–15297

Zhang Z, Cui J, Wang B, Jiang H, Chen G, Jinhong Y, Lin C, Tang C, Hartmaier A, Zhang J, Luo J, Rosenkranz A, Jiang N, Guo D (2018a) In situ TEM observation of rebonding on fractured silicon carbide. Nanoscale 10:6261–6269

Zhang Z, Shi Z, Yuefeng D, Zhijian Y, Guo L, Guo D (2018b) A novel approach of chemical mechanical polishing for a titanium alloy using an environment-friendly slurry. Appl Surf Sci 427:409–415